Phase behavior and fluid–solid surface tension of argon in slit pores and carbon nanotubes

Yoshinobu Hamada, Kenichiro Koga *, Hideki Tanaka

Department of Chemistry, Faculty of Science, Okayama University, Okayama 700-8530, Japan

ARTICLE INFO

ABSTRACT

Phase behaviors of argon in several types of cylindrical and slit pores are examined by grand-canonical Monte Carlo simulations. Condensation processes in single- and multi-walled carbon nanotubes along with those in hard-wall tubes are compared. Effects of the pore size on pressure–tensor components, the fluid–wall surface tension, and the adsorption are also compared for the different fluid-pore interactions. The chemical potential at which the fluid begins to condense in the single-walled nanotube is greater than that in the multi-walled nanotube by an amount nearly equal to the difference in the potential-well depth of the fluid-pore interaction, and the adsorption isotherms overlap each other almost completely for narrow pores and partially for wider pores. Similar analyses are performed for slit pores of two different hydrocarbon models.

1. Introduction

Structure and phase behavior of a fluid under extreme confinement are often much richer than those of the bulk fluid. The confined system is more complex in that its properties depend not only on the thermodynamic field variables such as the temperature and chemical potential but also on additional variables: e.g., the pore materials and geometry [1–4].

When the pore size is much larger than the size of particles, structures of the fluid and solid far from the pore walls are essentially identical to those of the bulk and a change in phase-equilibrium conditions is often described by a first-order term of the expansion of the thermodynamic variable with respect to the inverse of pore size. Examples are the Kelvin equation for the condensation pressure [2] and the Gibbs–Thomson equation for the melting-point depression [4]. But when the pore size is as small as several times the particle diameter, fluid properties including phase equilibrium conditions are qualitatively different from the bulk [5–8].

In the large-pore regime the pressure in the pore is well-defined as a scalar variable: call it P_{pore}. The pressure outside the pore is the equilibrium bulk pressure: call it P_{bulk}. When the fluid is in the same phase (liquid or gas) in and outside the pore, the corresponding pressures are the same: $P_{pore} = P_{bulk}$. When the fluid is in different phases, say α and β, in and outside the pore, $P_{pore} \neq P_{bulk}$ at given T and μ except at the bulk-phase equilibria. As special cases, when two phases coexist *in* the pore, e.g., at capillary condensation or freezing, the pressure difference $P_{pore} - P_{bulk}$ is given by Laplace's equation. The relation between P_{pore} and P_{bulk} remarked above remains the same for any size of pore in the large-pore regime, and the fluid–fluid and fluid–wall surface tensions are independent of the pore size. These are in fact necessary ingredients for the derivation of the Kelvin and Gibbs–Thomson equations. In the small-pore regime, on the other hand, the pressure is not a scalar but is a tensor. There is no bulk-like region in the confined fluid and so, in principle, the fluid phase in and outside the pore cannot be the same even if both are condensed phases. Therefore any component of the pressure tensor is different

* Corresponding author.
E-mail address: koga@cc.okayama-u.ac.jp (K. Koga).

from P_{bulk} and the difference of any pressure–tensor component from P_{bulk} at two-phase equilibria is not given by Laplace's equation. The fluid–fluid and fluid–wall surface tensions are dependent on the pore size in this regime.

Another difference between large- and small-pore regimes is the effect of the fluid-pore interaction (e.g., hydrophobic or hydrophilic, strongly repulsive or attractive, etc): in the large pores the general pictures described above, including Kelvin and Gibbs–Thomson equations, hold for for any types of the fluid-pore interaction; however in the small-pore regime the phase behavior may be qualitatively different for different types of pore surface.

Here we examine effects of the pore size, pore geometry, and fluid-pore interaction on the phase behavior of a simple liquid. We perform grand-canonical Monte Carlo simulations of argon in single- and multi-walled carbon nanotubes and of argon in slit pores made of a solid hydrocarbon. We focus on the phase behaviors in the small-pore regime and compare isothermal adsorption/desorption for the non-attractive hard-wall and attractive soft-wall pores.

2. Models and simulation methods

2.1. System and potential function

Properties of a fluid confined in a pore of volume V at given temperature T and chemical potential μ are obtained by the grand-canonical ensemble Monte Carlo (GCMC) simulation [9,10]. We implement the GCMC simulations of the Lennard–Jones (LJ) fluid in the model slit pore and carbon nanotubes, and obtain the density, pressure–tensor components, and the fluid–solid surface tension as functions of μ, or bulk pressure P_{bulk}, T, and the pore size. The corresponding bulk properties are obtained by the GCMC simulation or a well-established equation of state for the LJ fluid [11].

The intermolecular interaction between fluid particles is taken to be the LJ potential function with a cut-off:

$$u(r) = \begin{cases} 4\varepsilon \left[\left(\dfrac{\sigma}{r}\right)^{12} - \left(\dfrac{\sigma}{r}\right)^{6} \right] & (r \leq 5\sigma) \\ 0 & (r > 5\sigma) \end{cases} \tag{1}$$

where ε and σ are the energy and size parameters for argon ($\varepsilon/k = 120$ K with k the Boltzmann constant; $\sigma = 3.4$ Å) and r the intermolecular distance. Periodic boundary conditions are imposed in one, two, and three directions, respectively, for the cylindrical-pore, slit-pore, and bulk systems. The reduced temperature $T^* = kT/\varepsilon$ is changed stepwise with an interval of 0.1. The reduced configurational chemical potential $\mu_c^*(\rho^*, T^*)$, defined by $\mu^*(\rho^*, T^*) - \mu_{\text{id}}^*(\rho^* = 1, T^*)$ the difference of the reduced chemical potential from that of the ideal gas of $\rho^* = 1$, is increased or decreased stepwise with an interval of 0.05 or 0.1. The mass of argon $m = 6.63 \times 10^{-26}$ kg is employed so that μ_c^* is converted to μ^*. At each thermodynamic state, 20×10^6 to 500×10^6 configurations are generated and 20×10^6 to 1.5×10^9 configurations are used for averaging. The thermodynamic conditions examined are listed in Table 1.

For both cylindrical and slit pore systems, hard-wall and soft-wall potentials are examined. As in the previous study [12] the hard-wall potential for the cylindrical pore is taken to be

$$\phi(r) = \begin{cases} \varepsilon_{\text{w}} & r \leq (D - \sigma)/2 = R - \sigma/2 \\ \infty & \text{otherwise} \end{cases} \tag{2}$$

where D is the diameter of the cylindrical pore and r the distance of a particle from the cylinder axis, and the corresponding potential for the slit pore is

$$\phi(z) = \begin{cases} \varepsilon_{\text{w}} & \text{if } |z| \leq (h - \sigma)/2 \\ \infty & \text{otherwise} \end{cases} \tag{3}$$

where h is the width of the slit pore and z the distance of a particle from the mirror plane of the slit pore. For these hard-wall systems, the strength of effective attractive interaction between the pore and a fluid particle is represented by the uniform potential field ε_{w}.

These hard-wall systems are compared with more realistic fluid-pore systems: argon adsorbed in carbon nanotubes and in slit pores of hydrocarbons. For the former systems, both single- and multi-walled nanotubes are examined. The potential ϕ for an interaction between a fluid molecule and the multi-walled carbon nanotube of n layers is given by integrating the argon–carbon LJ potential over a single carbon layer [13] and then summing the integrated potential over the n layers. The result is written as

$$\phi(r) = \pi^2 \rho_{\text{w}} \varepsilon_{\text{w}} \sigma_{\text{w}}^2 \sum_{i=1}^{n} \left\{ \frac{63}{32} \frac{1}{\left[\frac{R_i - r}{\sigma_{\text{w}}} \left(1 + \frac{r}{R_i}\right) \right]^{10}} F\left[-\frac{9}{2}, -\frac{9}{2}; 1; \left(\frac{r}{R_i}\right)^2 \right] \right.$$

$$\left. - 3 \frac{1}{\left[\frac{R_i - r}{\sigma_{\text{w}}} \left(1 + \frac{r}{R_i}\right) \right]^{4}} F\left[-\frac{3}{2}, -\frac{3}{2}; 1; \left(\frac{r}{R_i}\right)^2 \right] \right\} \tag{4}$$

Table 1
Pore types, sizes, and ranges of thermodynamic states examined by the GCMC simulations. The interval of T^* is 0.1 and that of μ_c^* is 0.05 or 0.1.

System	Interaction	Pore size	T^*	$\mu_c^* \equiv T^* \ln z^*$
Cylindrical	Hard wall	$D^* = 2$	0.6 to 1.0	−4.9 to 4.9
		3	1.0	−4.9 to 4.9
		5	0.7 to 1.0	−4.9 to 4.9
		11	0.8 to 1.2	−4.0 to 4.0
	Single walled	$D^* = 2$	0.3 to 1.0	−15.8 to −5.0
		3	1.0	−12.85 to 0.0
		4	0.8 to 1.0	−13.75 to −6.75
		5	0.5 to 1.0	−11.55 to 0.0
		11	1.0	−11.15 to −4.0
	Multi walled	$D^* = 2$	0.9 to 1.1	−14.95 to 0.0
		3,4	1.0	−12.2 to −6.2
		5	0.9 to 1.1	−14.95 to 0.0
		11	0.9 to 1.1	−12.5 to −2.0
Slit	Hard wall	$h^* = 2$	0.7 to 1.1	−4.45 to 4.9
		3	1.0	−2.65 to 4.8
		5	0.9 to 1.3	−4.0 to 4.9
		11	0.9 to 1.2	−4.0 to 4.0
	9-3potential	$h^* = 2$	1.0	−4.8 to 4.9
		3,4	1.0	−4.2 to −0.2
		5	1.0	−5.3 to 0.0
		11	1.0	−5.9 to 2.7
	10-4-3potential	$h^* = 2$	1.0	−5.0 to 0.0
		3,4	1.0	−4.2 to −0.2
		5	1.0	−5.45 to −0.4
		11	1.0	−6.05 to 0.0
Bulk			0.8 to 1.3	−4.9 to 4.9

where ρ_w is the surface number density of carbon atoms in a graphite sheet, ε_w the energy parameter for the argon–carbon LJ potential, r the distance of the fluid molecule from the tube axis, and $R_i = R + (i-1)\Delta R$ the radius of the i-th carbon layer with R the radius of the innermost carbon layer and ΔR the distance between neighboring layers [14]. The $F(a, b; c; x)$'s are the hypergeometric functions with parameters a, b, and c, which result from the integration of the LJ potential over a cylindrical surface. The summation with respect to i indicates the sum over n layers.

Two potential models are studied for the soft slit-pore system. One is the 9-3 LJ potential [15]:

$$\phi(z) = \frac{2\rho_v \varepsilon_w \sigma_w^3}{3} \left[\frac{2}{15} \left(\frac{\sigma_w}{z} \right)^9 - \left(\frac{\sigma_w}{z} \right)^3 \right] \tag{5}$$

for the interaction between an argon atom and a single wall of density ρ_v. This form results from integrating the 12-6 LJ potential with respect to the coordinates of a volume element of the wall over the infinite volume. Here we have chosen $\rho_v^* \varepsilon_w^* = 0.6945$ [16] and $\sigma_w = 3.461$ Å. The other model is the 10-4-3 LJ potential [15]:

$$\phi(z) = \pi^2 \rho_w \varepsilon_w \sigma_w^2 \left[\frac{2}{5} \left(\frac{\sigma_w}{z} \right)^{10} - \left(\frac{\sigma_w}{z} \right)^4 - \frac{\sigma_w^4}{3\Delta z (z + 0.61\Delta z)^3} \right], \tag{6}$$

which is the superposition of single-sheet potentials with the interval of $\Delta z = 0.968\sigma_w$ [15] and the particular value $\rho_w^* \varepsilon_w^* = 0.8816$ for a hydrocarbon material [16].

For the cylindrical-pore system, the simulation cell is of length $L^* = L/\sigma = 200$ and diameter $D^* = D/\sigma = 2, 3, 4, 5, 11$. The surface area A is defined as πDL. The volume V of the pore is defined as $\pi (D/2)^2 L$. For the slit-pore system, the simulation cell is a square prism with an edge $L^* = 20$ and a height $h^* = h/\sigma = 2, 3, 4, 5, 11$. The "total" surface area A is $2L^2$. The volume V of pore is defined as hL^2.

It was noted earlier [12] that the thermodynamic state of a hard-wall pore system with a uniform potential ε_w at given T and μ is equivalent to the state of a hard-wall pore system with no attraction ($\varepsilon_w = 0$) at the same T and different chemical potential $\mu' = \mu - \varepsilon_w$.

2.2. Pressure and pressure tensor

It was noted above that the pressure of inhomogeneous fluids is no longer a scalar quantity but a tensor. It is not obvious and has not been systematically studied how a component of the pressure tensor of an inhomogeneous fluid is related to P_{bulk} in equilibrium. We examine a component parallel with the axis of a cylindrical pore or parallel with the slit-pore surfaces and call it $P_{\parallel}$. The pressure of the LJ fluid is given accurately by the empirical equation of state [11]. The pressure–tensor

component $P_\parallel$ is given by the virial in that direction

$$P_\parallel = \begin{cases} \rho_{\text{pore}}kT + \dfrac{1}{V}\left\langle \displaystyle\sum_{i<j}(z_{ij}f_{ij}^z)\right\rangle, & \text{(cylindrical pore)} \\[2ex] \rho_{\text{pore}}kT + \dfrac{1}{2V}\left\langle \displaystyle\sum_{i<j}(x_{ij}f_{ij}^x + y_{ij}f_{ij}^y)\right\rangle, & \text{(slit pore)}, \end{cases} \tag{7}$$

where V is the volume of the pore, N_{pore} the number of fluid particles in the pore, and $\rho_{\text{pore}} = N_{\text{pore}}/V$ the number density of the fluid.

2.3. Fluid-wall surface tension

An infinitesimal change dU in energy of a fluid in a slit pore may be written as

$$dU = TdS + \mu dN - P_\parallel(h/2)dA - P_\perp(A/2)dh \tag{8}$$

where S is the entropy, A is the total area of the fluid–wall interfaces, $P_\parallel = -(2/h)(\partial U/\partial A)_{S,N,h}$, and $P_\perp = -(2/A)(\partial U/\partial h)_{S,N,A}$. There is arbitrariness in the choice of the position of the dividing surfaces by which the pore and the surrounding wall are separated. Thus, in cases of slit pores, the width h has the corresponding arbitrariness on a microscopic scale, and so does the pressure–tensor component $P_\parallel$. To be more specific, since $P_\parallel h/2$ is independent of the choice of h, a change in $P_\parallel$ that follows from a notional change $[dh]$ in h is given by the relation $P_\parallel \sim 1/h$ [12]. The notional dependence of $P_\parallel$ becomes negligible when h is much greater than σ.

The fluid–wall surface tension γ may be defined as

$$\gamma = \frac{1}{2}h(P_{\text{bulk}} - P_\parallel) \tag{9}$$

so that

$$dU = TdS + \mu dN + \gamma dA - P_{\text{bulk}}(h/2)dA - P_\perp(A/2)dh. \tag{10}$$

This definition of γ follows from the same idea as proposed by Gibbs [17,18]. The tension γ is also dependent on the choice of h:

$$[\Delta\gamma] = \frac{1}{2}P_{\text{bulk}}[\Delta h], \tag{11}$$

where the differences in square brackets denote the notional changes. The notional dependence of γ on the choice of h is insignificant if P_{bulk} is small and h is chosen in a microscopic range.

The same thermodynamic arguments as described above apply to the cylindrical-pore systems. The fluid–wall tension is given by

$$\gamma = \frac{1}{2}R(P_{\text{bulk}} - P_\parallel) \tag{12}$$

and γ depends on the choice of R as

$$[\Delta\gamma] = \frac{1}{2}[\Delta R]\left(P_{\text{bulk}} + \frac{P_\parallel}{1 + [\Delta R]/R}\right). \tag{13}$$

The adsorption Γ for any types of pore in general is the excess number of adsorbate molecules in the pore per unit area defined as

$$\Gamma = \frac{1}{A}(N_{\text{pore}} - N_{\text{bulk}}) = \frac{V}{A}(\rho_{\text{pore}} - \rho_{\text{bulk}}). \tag{14}$$

This quantity is directly obtained from the GCMC simulation, and also related to the surface tension through the adsorption equation:

$$\Gamma = -\left(\frac{\partial\gamma}{\partial\mu}\right)_T. \tag{15}$$

In the case of a slit or cylindrical pore, Eq. (15) together with the definition of γ, (9) or (12), leads to (14) with appropriate A and V for each geometry.

3. Results and discussions

3.1. Phase behavior in cylindrical pores

Effects of the pore diameter on the phase behavior of the confined fluid (argon) are examined for single- and multi-walled carbon nanotubes together with purely-repulsive hard-wall tubes. Fig. 1 shows three kinds of isotherms for three diameters $D^* = 2, 5$, and 11 at $T^* = 1.0$. In Fig. 1(a)–(c) the logarithm of $P_\parallel$ is plotted against μ^*/T^*: its slope approaches 1 in the
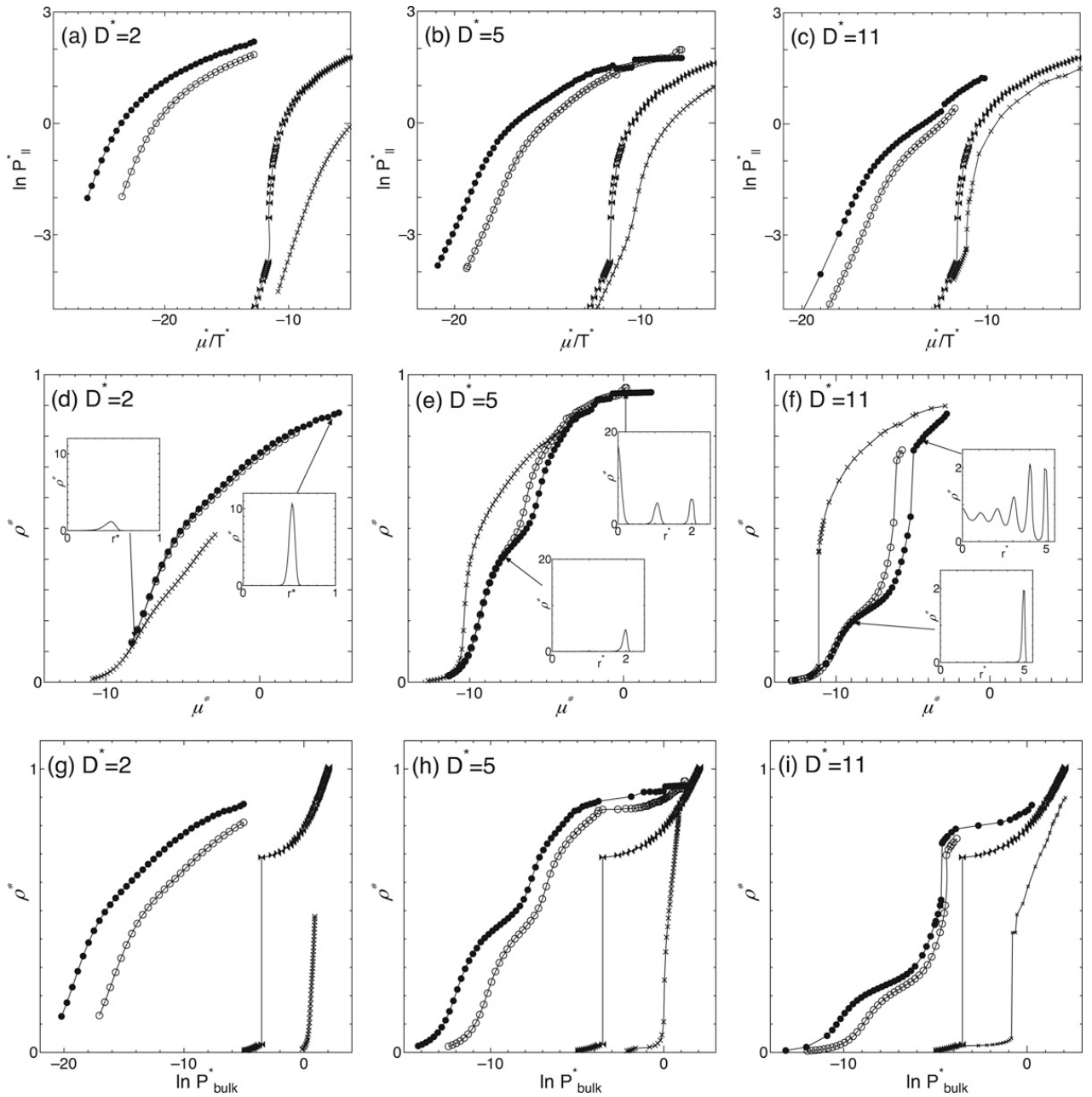
Fig. 1. Isotherms $\ln P_{\parallel}^*$ vs. μ^*/T^* [(a)–(c)], ρ_{pore}^* vs. μ^* [(d)–(f)], and ρ_{pore}^* vs. $\ln P_{\text{bulk}}^*$ [(g)–(i)] for argon in model carbon nanotubes and hard-wall pores. The fixed dimensionless temperature $T^* = 1.0$. The pore diameter D^* is given in the figures. Filled circles: multi-walled nanotube; open circles: single-walled nanotube; crosses: hard-wall cylindrical pore; ribbons: bulk. The insets show the density profiles at the points marked by arrows.

ideal-gas limit (small $P_{\parallel}$, small μ^*/T^* states). In Fig. 1(d)–(f) the ρ_{pore} vs. μ^* curves for the single- and multi-walled carbon nanotubes are shifted laterally to the direction of increasing μ^* such that the point on each isotherm of lowest ρ_{pore} coincides with that of the same ρ_{pore} of the hard-wall pore. In Fig. 1(g)–(i) the adsorption isotherms ρ_{pore} vs. $\ln P_{\text{bulk}}^*$ are plotted.

As μ^* is increased, or the bulk pressure is increased, condensation occurs in the order of multi-walled nanotubes, single-walled nanotubes, and hard-wall pores, i.e., in the order of strength of the fluid–wall attractive interaction. The isotherm for the bulk system lies between that for the single-walled nanotube and that for the hard-wall pore: that is, the fluid exhibits capillary condensation in the single- and multi-walled nanotubes and capillary evaporation in the hard-wall pore.

In cases of $D^* = 2$, the narrowest pore examined, the fluid condensates gradually with no steep change of ρ_{pore}; see Fig. 1(g). In the pores of medium size ($D^* = 5$), condensation is continuous but is accompanied by distinct two-step changes in ρ_{pore} in the single- and multi-walled carbon nanotubes; see Fig. 1(h). It is confirmed from corresponding changes in the density profile that the two-step change in ρ_{pore} reflects the formation of a single layer along the pore wall followed by filling of the hollow space; see the insets in Fig. 1(e). The stepwise filling process is not observed for the purely-repulsive hard-wall pore of the same diameter. In the widest pores examined, the two-step filling process is found again for the attractive soft pores while a single, almost discontinuous change in ρ_{pore} is found for the hard-wall pore.
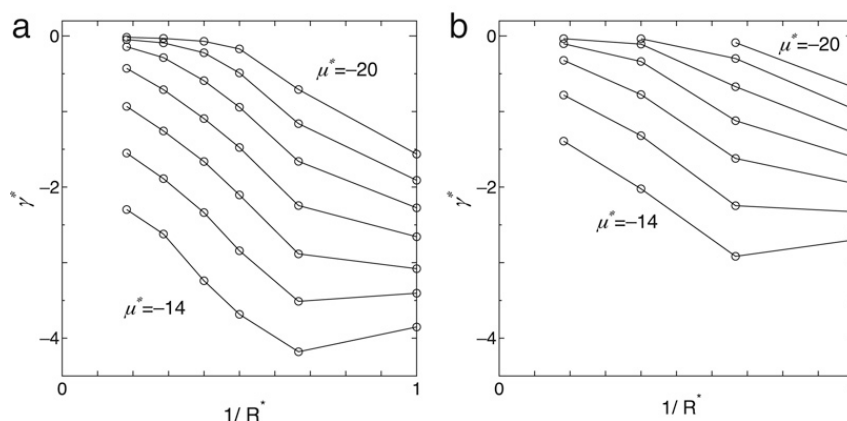
Fig. 2. The fluid–wall surface tension γ vs. $1/R^*$ in (a) multi-walled and (b) single-walled nanotubes at $T^* = 1.0$. The fixed chemical potential μ^* for each curve is $-14, -15, \ldots, -20$ from the bottom curve to top.

Remember that each ρ_{pore}-μ^* isotherm for the single- and multi-walled nanotubes is shifted laterally such that the lowest ρ_{pore} point on the isotherm coincides with that of the hard-wall pore. In the case of $D^* = 2$, the two isotherms of the single- and multi-walled nanotube systems almost perfectly overlap with each other over the entire range of continuous condensation. In the other cases $D^* = 5$ and 11, the two isotherms coincide very well with each other over the range corresponding to the first step of condensation (formation of a liquid-like layer), and then they separate from each other as the second, filling process proceeds. These results indicate that the isothermal adsorption curve (or a part corresponding to the first step of adsorption) of argon in a single-walled nanotube is essentially identical to the one in a multi-walled nanotube of the same diameter *except* that the former is displaced from the latter by $\Delta\mu^*$.

The values of $\Delta\mu^*$ are 2.80, 1.60, and 1.30 for $D^* = 2$, 5, and 11. The difference $\Delta\mu^*$ in the chemical potential at which the fluid begins to condense arises from the different fluid-nanotube interactions. The multi-walled carbon nanotube has a deeper potential well than that of the single-walled nanotube of the same diameter: the difference $\Delta\varepsilon^*_{min}$ in the potential-well depth ε^*_{min} is 2.78, 1.67, and 1.34 for $D^* = 2$, 5, and 11. We note that $\Delta\mu^* \simeq \Delta\varepsilon^*_{min}$ for each diameter. That is to say, the difference in the initial stage of adsorption (or the entire condensation process in the case of the narrowest nanotube) is merely the chemical potential shift equivalent to the difference in the fluid-nanotube interaction potential at its minimum.

The adsorption curves for the hard-wall pores do not overlap with those for the carbon nanotubes. However, the displacement $\Delta\mu^*$ (with respect to the lowest ρ_{pore} examined) of the adsorption isotherm for single- and multi-walled nanotubes from that for the hard-wall pore is closely related to the depth ε_{min} of the potential well for each nanotube: in the cases of the multi-walled nanotubes of $D^* = 2$, 5, and 11, $\Delta\mu^*$ is 18.0, 9.6, and 7.4 and $\varepsilon^*_{min} = 18.4$, 11.7, and 10.1, respectively. The larger the diameter D, the larger the discrepancy between $\Delta\mu^*$ and ε^*_{min}.

In the second stage of adsorption for $D^* = 5$ and 11 where the entire hollow space of the nanotube is filled with the liquid, we notice, the shifted adsorption isotherm for the single-walled nanotube deviates from that for the multi-walled nanotube to the direction of lower μ^*. This is because the height of the potential maximum (at the tube axis) measured from its minimum is lower in the single-walled nanotube than in the multi-walled nanotube. Thus the density in the pore increases more rapidly in the single-walled nanotube than in the multi-walled nanotube by increasing μ^*.

3.2. Surface tension and adsorption in cylindrical pores

Dependence of the fluid-pore wall surface tension γ on the pore radius R is of particular interest. In the previous study it was found for the LJ fluid in the hard-wall pore that γ decreases linearly with $1/R$ at fixed T and μ [12]. Fig. 2 shows how γ depends on $1/R$ at $T^* = 1.0$ and at $\mu^* = -20, -19, \ldots, -14$. The range over which γ varies linearly with $1/R$ is limited compared to that in the hard-pore system. A near-linear relation between γ and $1/R$ holds over a diameter range from $D^* = 3$ to 11 for fixed μ^* greater than -17 and over a range from $D^* = 2$ to 4 for relatively-low μ^* ($\mu^* = -20, -19$), as shown in Fig. 2a in cases of the multi-walled nanotube systems. Similar near-linear relation holds for the single-walled nanotube systems (Fig. 2b).

The fluid–wall surface tension γ can be either positive or negative unlike the surface tension at fluid interfaces. The sign of γ is determined by an inequality between P_{bulk} and $P_{\parallel}$, the equilibrium pressure in bulk and the pressure–tensor component parallel with the pore surface: see Eq. (9) or (12). It is negative if $P_{\parallel}$ exceeds P_{bulk}, and that is what we find in the single- and multi-walled carbon-nanotube systems (Fig. 2). In the cases of hard-wall pore systems we have observed [12] that γ is positive, that is, $P_{\parallel}$ is lower than P_{bulk}. The inequalities, $P_{\parallel} > P_{bulk}$ for the nanotube systems and $P_{\parallel} < P_{bulk}$ for the hard-wall pore systems, are in turn related to the phase equilibrium between the fluids in pore and bulk: the fluid in the nanotubes at given μ^* and T^* in Fig. 2 is as dense as a liquid while that in bulk is gaseous ($\rho_{pore} > \rho_{bulk}$); for the hard-wall pores, however, the confined fluid is less dense than in the bulk.
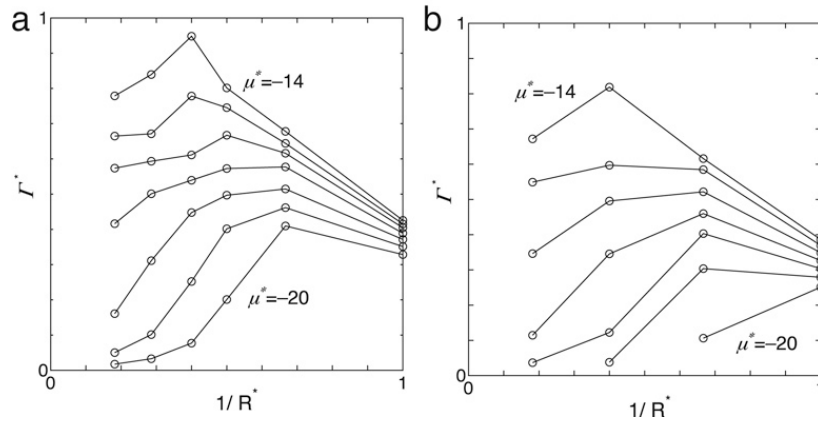
Fig. 3. The adsorption Γ^* vs. $1/R^*$ in the (a) multi-walled and (b) single-walled carbon nanotubes at $T^* = 1.0$. The fixed chemical potential μ^* for each curve is $-14, -15, \ldots, -20$ from the top curve to bottom.

Now compare γ in the multi-walled, single-walled, and hard-wall nanopores at common μ, T, and D. One finds that γ in the multi-walled pore is lowest and that in the hard-wall pore is highest. This means that $P_\parallel(\text{multi-walled}) > P_\parallel(\text{single-walled}) > P_\parallel(\text{hard-wall})$.

Also seen in Fig. 2 is that γ in the nanotube systems decreases with increasing μ (and so with increasing P_{bulk}) at fixed D^*. This is consistent with the adsorption Γ being positive in the range of μ as shown in Fig. 3, for the derivative of γ with respect to μ is the negative of Γ [the adsorption Eq. (15)]. An opposite trend was found in the cases of hard-wall pore systems [12] where $\Gamma < 0$ and thus $(\partial\gamma/\partial\mu)_T > 0$.

The adsorption Γ is a non-monotonic function of the pore diameter D as shown in Fig. 3. In the range of μ^* at $T^* = 1.0$, the bulk fluid is always in a gaseous state while the fluid in the nanotube is in-between gaseous or liquid-like states, so $\Gamma > 0$. With increasing D^* from the narrowest to widest, Γ first increases and then turns to decrease. This non-monotonic behavior of Γ is explained as follows. As long as the pore is filled with the fluid molecules, then Γ would increase monotonically as the diameter increases because the bulk phase is a gas. That happens for $D^* \leq 5$ or $1/R^* \geq 0.4$ at $\mu^* = -14$ as shown in Fig. 3. But when the diameter is greater than a certain value, the pore is not completely filled with the fluid. Then Γ decreases as D^* increases. Why is the pore filled completely for smaller diameters and incompletely filled or empty except an adsorption layer for larger diameters? It is because the smaller the diameter the lower the potential energy that a fluid molecule feels around the axis of the cylindrical pore. For example, the value for the multi-walled nanotube is about $-kT$ for $D^* = 5$ while it is nearly zero for $D^* = 11$. The adsorption is greater in the multi-walled nanotube than in the single-walled nanotube at the same μ, T, and D because the attractive potential well is deeper in the former system.

3.3. Phase behavior in slit pores

Fig. 4 shows three kinds of isotherm, $\ln P_\parallel^*$ vs. μ^*/T^* [Fig. 4(a)–(c)], ρ_{pore} vs. μ^* [Fig. 4(d)–(f)], and ρ_{pore} vs. $\ln P_{\text{bulk}}^*$ [Fig. 4(g)–(i)], for the three types of slit pore: the 10-4-3 LJ, 9-3 LJ, and hard-wall potentials. The fixed temperature is $T^* = 1.0$. As in Fig. 1(d)–(f) the ρ_{pore} vs. μ^* curves for the 10-4-3 and 9-3 LJ slit pores are shifted laterally to the direction of increasing μ^* such that the point on each isotherm of lowest ρ_{pore} coincides with that of the same ρ_{pore} of the hard-wall pore.

In any pores of $h^* = 2.0$, condensation takes place continuously as shown in Fig. 4(g); but the density change is more rapid in the slit than in the cylindrical pores of the same size ($D^* = 2$). It is also clear in Fig. 4(d) that the shifted ρ_{pore} vs. μ^* curves for the two models of the attractive soft-wall pore closely overlap with each other, that is, the adsorption curves for the two models are almost identical except the lateral displacement $\Delta\mu^*$. They do not, however, overlap with the adsorption curve for the hard-wall pore. The value of $\Delta\mu^*$ is 0.9 while $\Delta\varepsilon_{\text{min}}^*$ is 1.2, so the shift in adsorption curve is mainly due to the difference in depth of the fluid–wall potential well.

In wider slit pores of $h^* = 5$ and 11, condensation is observed as a first-order phase transition. In contrast to the adsorption in carbon nanotubes, it takes place as a single step with no monolayer formation. This is due to the fact that the potential well for the fluid-pore interaction is about four times deeper for the nanotubes than for the model slit pores.

The chemical potential or the bulk pressure at which capillary condensation takes place is very close to that for the bulk condensation. For example, in the 9-3 LJ potential pore of $h^* = 11$, the transition μ^* is almost identical to that in bulk; see Fig. 4(i).

The displacement $\Delta\mu^*$ of the adsorption curve for the attractive soft-wall pores from that for the non-attractive hard-wall pore is nearly equal to the depth $\varepsilon_{\text{min}}^*$ of the attractive potential well when $h^* = 2.0$. But that is not the case for the wider pores. For example, in the 10-4-3 LJ potential pores of $h^* = 2$, 5, and 11, $\Delta\mu^*$ is 3.0, 1.4, and 0.8 and $\varepsilon_{\text{min}}^* = 3.3$, 3.0, and 3.0, respectively.
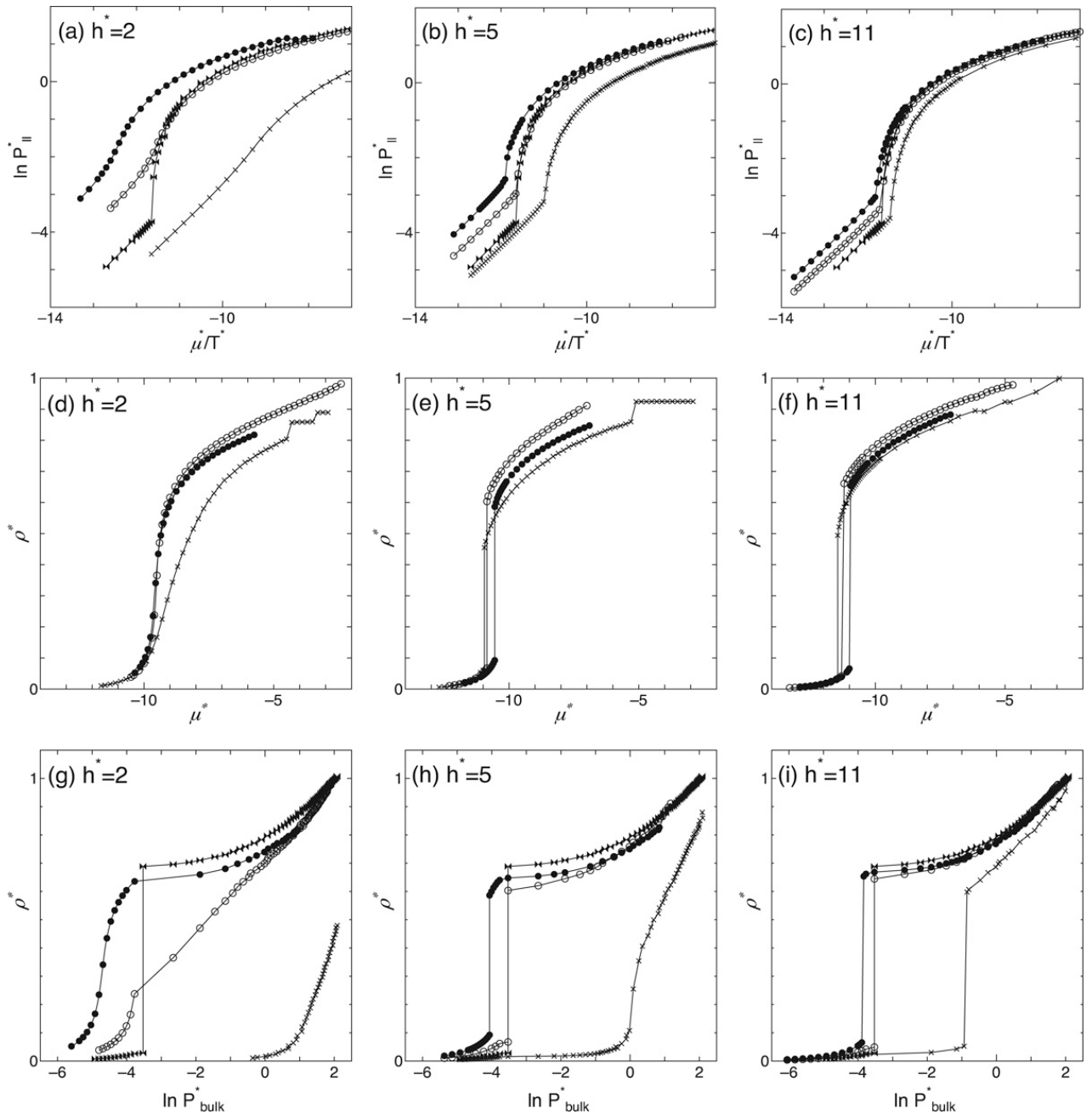
Fig. 4. Isotherms $\ln P_{\parallel}^*$ vs. μ^*/T^* [(a)–(c)], ρ_{pore}^* vs. μ^* [(d)–(f)], and ρ_{pore}^* vs. $\ln P_{bulk}^*$ [(g)–(i)] for argon in the three kinds of slit pores. The fixed dimensionless temperature $T^* = 1.0$. The pore width h^* is given in the figures. Filled circles: the 10-4-3 LJ potential slit; open circles: the 9-3 LJ potential slit; crosses: the hard-wall slit; ribbons: bulk.

A notable difference between the 10-4-3 LJ and 9-3 LJ potential systems is found at condensation where a gaseous fluid and a liquid coexist in the slit pore. At the two-phase equilibrium in each pore the density difference between the two phases is greater in the 9-3 LJ pore than in the 10-4-3 LJ pore: the gas density is lower and the liquid density is higher in the 9-3 LJ pore than in the 10-4-3 LJ pore. This is due to that the height of the potential maximum at the mid point of the pore than in the 10-4-3 LJ pore.

3.4. Surface tension and adsorption in slit pores

The surface tension γ and the adsorption Γ for the slit-pore systems are given in Figs. 5 and 6. They are plotted as functions of the inverse of pore width, $1/h^*$. The temperature T^* is fixed at 1 and the chemical potential at several different values in a rather small range, $-12 < \mu^* < -11$. We have chosen this range because we are interested in the behavior of γ and Γ when a gas–liquid phase change takes place either in the slit pores or in bulk: in this range of μ^*, the fluid in the slit pores of $h^* = 5$ and 11 and in bulk exhibits the first-order gas–liquid phase transition while the fluid in the slit of $h^* = 2$ shows continuous condensation. The gas–liquid equilibrium μ^* for the bulk fluid is close to -11.65.
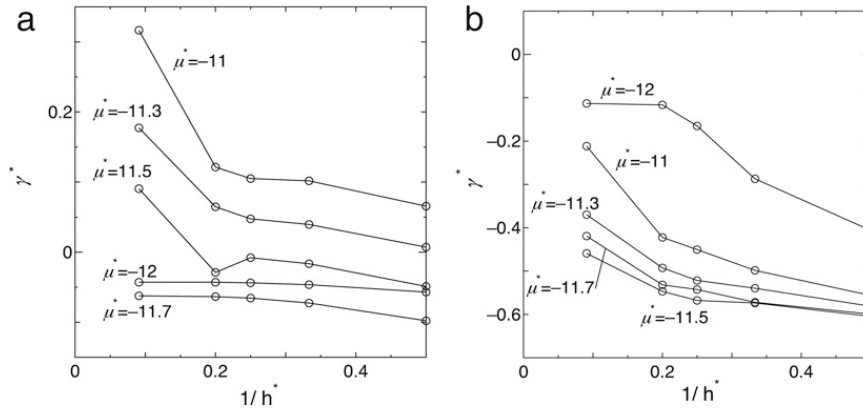
Fig. 5. The fluid–wall surface tension γ^* vs. $1/h^*$ in (a) 9-3 and (b) 10-4-3 LJ potential slits at $T^* = 1.0$. The fixed chemical potential for each curve is indicated in the figures.
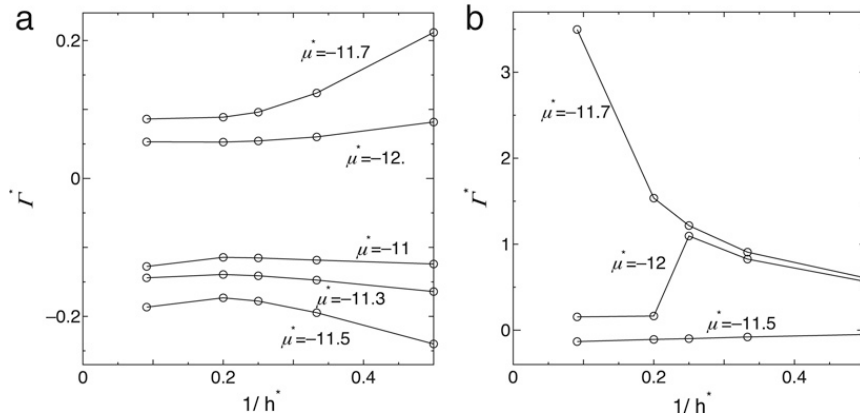
Fig. 6. The adsorption Γ^* vs. $1/h^*$ in (a) 9-3 LJ and (b) 10-4-3 LJ potential slits at $T^* = 1.0$. The fixed chemical potential for each curve is indicated in the figures.

In the 9-3 LJ slit-pore systems, the fluid is gaseous when $\mu^* < -11.65$ and liquid-like otherwise. Behaviors of γ and Γ in the former regime are different from those in the latter regime. In the former, the fluid both in and outside the pore is gaseous, $P_{bulk} - P_{\parallel}$ is negative and small in magnitude, and $\rho_{bulk} - \rho_{pore}$ is negative. In such circumstances the tension γ is negative and small in magnitude and the adsorption Γ is positive. With increasing μ at fixed h, γ becomes more negative and Γ becomes more positive. The dependence of γ on μ is consistent with $\Gamma > 0$. In the latter cases ($\mu^* > -11.65$), the fluid both in and outside the pore is liquid-like, $P_{bulk} - P_{\parallel}$ is positive and small in magnitude, and $\rho_{bulk} - \rho_{pore}$ is positive. In those conditions $\gamma > 0$ and $\Gamma < 0$, and γ increases with increasing μ, which is consistent with the adsorption Γ being negative. The Γ becomes less negative with increasing μ.

In the 10-4-3 LJ slit-pore systems, condensation of the gaseous fluid takes place at μ lower than in the 9-3 LJ slit-pore systems. This is because the depth of the fluid–wall potential well is deeper in the 10-4-3 LJ potential. In the range of μ examined, γ is negative, and it becomes more negative with increasing μ from -12 to -11.7 and then becomes less negative with further increasing μ. This behavior is consistent with the sign of Γ: in the former regime the fluid in bulk is a gas and Γ is positive while in the latter regime the fluid is liquid-like both in and outside the pore and Γ is negative.

Dependence of γ on the pore width h is much weaker in the slit-pore geometry than in the cylindrical geometry: compare Fig. 5 with Fig. 2. Dependence of Γ on $1/h$ for the 9-3 LJ slit pores is weak and nearly monotonic in contrast to that for the carbon nanotubes. Dependence of Γ for the 10-4-3 LJ slit pores is also weak at $\mu^* \geq -11.5$; however, at $\mu^* = -11.7$, Γ depends strongly on $1/h$ (specifically it looks inversely proportional to $1/h$). The weak dependence of Γ on $1/h$ is seen when the fluid both in and outside the pore is in the same phase and a strong dependence is found when the fluid is liquid-like in the pore while the bulk phase is gaseous. The reason is the following. When bulk and confined fluids are both liquid-like or gaseous, $N_{ex} \equiv (\rho_{pore} - \rho_{bulk})V \ll N_{pore}$ and so $\Gamma = N_{ex}/A$ is due to the adsorption *at* the surface of pore. Thus Γ depends only weakly on $1/h$. On the other hand, when a confined fluid is liquid-like and the equilibrium bulk phase is gaseous, $N_{ex} \simeq N_{pore}$ and so Γ is asymptotically proportional to h, or equivalently Γ is inversely proportional to $1/h$, which is found for the isotherm of $\mu^* = -11.7$ in Fig. 6b. The isotherm of $\mu^* = -12$ in Fig. 6b shows non-monotonic behavior. It is close to a curve inversely proportional to $1/h$ for $1/h^* > 0.25$ and is nearly constant and close to 0 for $1/h^* < 0.20$. This is because the fluid in the pore undergoes the liquid-to-gas phase change at some h as h is increased from 4 to 5.

4. Conclusions

We performed GCMC simulations to study condensation of argon in carbon nanotubes and hydrocarbon slit pores. Effects of the pore geometry, size, and type of the fluid-pore interaction on the phase behavior were examined.

At $T^* = 1.0$ or $T = 120$ K, condensation of an argon gas is continuous for all types of cylindrical pores (single- and multi-walled nanotubes and hard-wall tubes) when the pore diameter $D^* \leq 5$ but the sign of a discontinuous transition is present for $D^* = 11$. At the same temperature, for all types of slit pores (9-3 and 10-4-3 LJ potential slit pores and hard-wall slit pores), continuous condensation is observed only for the smallest diameter ($D^* = 2$); otherwise it is observed as a first-order phase transition.

Adsorption isotherms for the narrowest nanotubes are entirely smooth while those for the wider nanotubes exhibit a two-step change reflecting the formation of a single layer along the pore surface followed by filling of the hollow space. For the narrowest case the ρ^* vs. μ^* isotherms for the single- and multi-walled nanotubes differ only by the lateral displacement in μ^*. The displacement $\Delta\mu^*$ is found to be nearly equal to $\Delta\varepsilon^*_{\min}$ the difference in the fluid–wall potential-well depth. For the larger diameters, the same is true for parts of the adsorption curves corresponding to formation of a single layer. The result has an important implication for adsorption experiments. That is, the difference in the fluid-pore potential-well depth among various materials is evaluated from their ρ^* vs. μ^* adsorption isotherms.

For the attractive soft-wall pores of narrowest size (D^* or $h^* = 2$), the displacement $\Delta\mu^*$ of the adsorption curve from that for the non-attractive hard-wall pore is nearly equal to the depth $\varepsilon_{\min}$ of the attractive potential well. This result, too, would be an important implication for the experiments of nano pores, for the depth $\varepsilon_{\min}$ itself might be determined from the isotherm of the real system together with the isotherm of the hard-wall pore. The latter isotherm can be easily determined by simulation.

Dependences of the fluid–wall surface tension γ and the adsorption Γ on the pore size were examined. The size dependence, magnitude, and sign of γ and Γ were explained by the phase of the fluid in and outside the pore and the fluid-pore interaction. It was confirmed that the dependence of γ on μ is consistent with the Gibbs adsorption equation.

References

 [1] R. Evans, U. Marini Bettolo Marconi, J. Chem. Phys. 86 (1987) 7138.
 [2] R. Evans, J. Phys. Condens. Matter 2 (1990) 8989.
 [3] H.K. Christenson, J. Phys. Condens. Matter 13 (2001) R95.
 [4] C. Alba-Simionesco, B. Coasne, G. Dosseh, G. Dudziak, K.E. Gubbins, R. Radhakrishnan, M. Sliwinska-Bartkowiak, J. Phys. Condens. Matter 18 (2006) R15–R68.
 [5] M. Schoen, D.J. Diestler, Phys. Rev. E 56 (1997) 4427.
 [6] B. Coasne, R.J.M. Pellenq, J. Chem. Phys. 120 (2004) 2913.
 [7] K. Koga, H. Tanaka, J. Chem. Phys. 122 (2005) 104711.
 [8] K. Koga, G.T. Gao, H. Tanaka, X.C Zeng, Nature 412 (2001) 802.
 [9] J. Yao, R.A. Greenkorn, K.C. Chao, Mol. Phys. 46 (1982) 587.
[10] B.K. Peterson, K.E. Gubbins, Mol. Phys. 62 (1987) 215.
[11] J.J. Nicolas, K.E. Gubbins, W.B. Streett, D.J. Tildesley, Mol. Phys. 37 (1979) 1429.
[12] Y. Hamada, K. Koga, H. Tanaka, J. Chem. Phys. 127 (2007) 084908.
[13] G.J. Tjatjopoulos, D.L. Feke, J. Adin Mann, J. Phys. Chem. 92 (1988) 4006.
[14] J.-C. Charlier, J.P. Michen, Phys. Rev. Lett. 79 (1993) 1858.
[15] W.A. Steele, The Interactions of Gases with Solid Surfaces, Pergamon, New York, 1974.
[16] C.Y. Lee, J.A. McCammon, P.J. Rossky, J. Chem. Phys. 80 (1984) 4448.
[17] J.W. Gibbs, The Collected Works of J. Willard Gibbs, vol. 1, Longmans, Green, 1928.
[18] J.S. Rowlinson, B. Widom, Molecular Theory of Capillarity, Clarendon, Oxford, 1982.